DOI: https://doi.org/10.1016/j.apenergy.2017.09.030

Citation:

Ulazia, Alain, Jon Sáenz, Gabriel Ibarra-Berastegui, Santos J. González-Rojí, and Sheila Carreno-Madinabeitia. “Using 3DVAR Data Assimilation to Measure Offshore Wind Energy Potential at Different Turbine Heights in the West Mediterranean.” Applied Energy 208 (December 2017): 1232–1245. doi:10.1016/j.apenergy.2017.09.030.

Using 3DVAR data assimilation to measure offshore wind energy potential **at different turbine heights in the West Mediterranean** ☆

Alain Ulazia[a,*], Jon Sáenz[c,d], Gabriel Ibarra-Berastegui[d,b], Santos J. González-Rojí[c], Sheila Carreno-Madinabeitia[e]

[a] *Department of NE and Fluid Mechanics, University of Basque Country (UPV/EHU). Otaola 29, 20600 Eibar, Spain.*
[b] *Department of NE and Fluid Mechanics, University of Basque Country (UPV/EHU). Alda. Urkijo, 48013 Bilbao, Spain.*
[c] *Department of Applied Physics II, University of Basque Country (UPV/EHU). B. Sarriena s/n, 48940 Leioa, Spain.*
[d] *Joint Research Unit (UPV/EHU-IOE) Plentziako Itsas Estazioa, University of Basque Country (UPV/EHU). Areatza Hiribidea 47, 48620 Plentzia, Spain.*
[e] *Meteorology Area, Energy and Environment Division, TECNALIA RI, Basque Country, Spain*

Abstract

In this article, offshore wind energy potential is measured around the West Mediterranean using the WRF meteorological model without 3DVAR data assimilation (the N simulation) and with 3DVAR data assimilation (the D simulation). Both simulations have been checked against the observations of six buoys and a spatially distributed analysis of wind based on satellite data (second version of Cross-Calibrated Multi-Platform, CCMPv2), and compared with ERA-Interim (ERAI). Three statistical indicators have been used: Pearson's correlation, root mean square error and the ratio of standard deviations. The simulation with data assimilation provides the best fit, and it is as good as ERAI, in many cases at a 95% confidence level. Although ERAI is the best model, in the spatially distributed evaluation versus CCMPv2 the D simulation has more consistent indicators than ERAI near the buoys. Additionally, our simulation's spatial resolution is five times higher than ERAI. Finally, regarding the estimation of wind energy potential, we have represented the annual and seasonal capacity factor maps over the study area, and our results have identified two areas of high potential to the north of Menorca and at Cabo Begur, where the wind energy potential has been estimated **for three turbines at different heights** according to the simulation with data assimilation.

Keywords: Offshore wind energy potential, WRF, WRFDA, data assimilation, Mesoscale model, Fluid Mechanics

*I am corresponding author
Email addresses: alain.ulazia@ehu.eus (Alain Ulazia), jon.saenz@ehu.eus (Jon Sáenz),

1. Introduction

Table 1: Nomenclature

SAR	Synthetic Aperture Radar
WRF	Weather Research and Forecasting Model
WAsP	Wind Atlas Analysis and Application Program
3DVAR	Three-Dimensional Variational method
SST	Sea Surface Temperature
NOAA	National Oceanic and Atmospheric Administration
MERRA	Modern-Era Retrospective Analysis for Research and Applications
NCEP	National Centers for Environmental Prediction
ECMWF	European Centre for Medium-Range Weather Forecasts
CCMP	Cross Calibrated Multi-Platform
WRFDA	WRF with Data Assimilation
N simulation	Our WRF simulation without data assimilation
D simulation	Our WRF simulation with data assimilation
UTC	Universal Time Coordinated
RMSE	Root Mean Square Error
SD	Standard Deviation
MAE	Mean Average Error
z_0	Roughness of the sea
z	Height above sea level
H_s	Significant Wave Height
L_p	Peak Period Wavelength
CF	Capacity Factor
U	Wind velocity
D	Wind turbine diameter
U_n	Normalized wind velocity
ρ	Air density
P_R	Rated power of the wind turbine
AEP	Annual Energy Production
OM	Operation and Maintenance
LCOE	Levelised Cost of Energy
TLB	Tension-Leg-Buoy

The importance of offshore wind energy as an energy source is increasing, especially now that floating wind farms have become viable [1]. Siemens wind turbines have recently been tested in Stavanger (Norway) to increase our understanding of this technology implemented at the world's first floating wind farm: Statoil's HyWind Scotland pilot park [2]. The

gabriel.ibarra@ehu.eus (Gabriel Ibarra-Berastegui), santosjose.gonzalez@ehu.eus (Santos J. González-Rojí), sheila.carreno@tecnalia.com (Sheila Carreno-Madinabeitia)

sites available for founded turbines at sea are limited, and so floating offshore wind farms would increase the available area for harnessing wind energy, as the Scottish case indicates. This kind of wind farm could therefore be an interesting option for many countries [3, 4]. The mass implementation of floating wind farms is currently being throughly evaluated not only from a technological and resource assessment perspective, but also incorporating an economic assessment of turbines and their mooring systems [5].

A potential location requires an accurate estimation of wind energy potential. Accordingly, standard methodologies are being widely applied, although they can still be refined. Garrad et al. [6] first estimated the European offshore wind climate, even though at that time it was difficult to properly verify their findings because of the lack of systematized observed data [7]. More recently, Synthetic Aperture Radar (SAR) has been used on the ocean surface [8] and lakes [9]. It records a close agreement with observations. However, even the use of satellite SAR data has not solved the problem of calculating the wind speed at hub height. It is usually solved through the assumption of a simplistic logarithmic wind shear (Equation 3) [10, 11, 12, 13, 14].

Mesoscale meteorological modelling is a widely used method for evaluating wind potential. It provides a wind resource map [10, 11, 15], and has already been applied to coastlines on the Iberian Peninsula [14]. The mesoscale model's wind speed data should be verified properly before estimating the wind energy potential, and in the case of the ocean this involves comparing the model's results to a buoy's anemometer observations, remote sensing observations, or similar analyses [16]. A proper characterization of the wind resource is usually followed by a comprehensive evaluation of the economic, topographic and bathymetric data, as well as all the other technical aspects for the practical implementation of a wind farm [13, 14, 17].

In previous studies, the results provided by the advanced mesoscale Weather Research and Forecasting Model (WRF) have been successfully compared to observed offshore and onshore wind data. Its performance has been evaluated for different onshore or offshore wide areas [18, 19, 20, 21, 22, 23], and even for turbulence and wake studies around specific wind farms [24, 25]. **Additionally, WRF has been recently used for wind forecasting in short and lon-term, which currently constitutes a very important aspect of wind industry's electricity production and sales [26, 27, 28, 29].**

In onshore wind resource prediction, these studies show that the WRF mesoscale model performs well when it is coupled with microscale models such as WAsP (Wind Atlas Analysis and Application Program), carefully taking into account those areas with a complex topography [18].The grid nudging and integration times of the simulations have also been tested for WRF, and the results suggest that errors can be minimized by choosing a suitable numerical and physical configuration with high resolution terrain data [19]. WRF sensitivity to different planetary boundary layer parametrization schemes has also been studied, and the best onshore or offshore evaluation results are associated with specific parametrization schemes [20]. Furthermore, the differences in the simulations are significant in terms of wind energy production.

In another study [21], offshore wind data derived from satellites (CCMP, QuikSCAT, NCDC Blended Sea Winds and IFREMER Blended Wind Fields), reanalyses (NCEP-CFSR,

ERA-Interim, NASA-MERRA and NCEP-RII), analyses (NCEP-FNL and NCEP-GFS) and WRF modeled offshore winds have been compared to observations from five buoys moored along the Iberian coastline. In the experiment, WRF outperforms the rest at reproducing observed offshore winds.

The performance of the WRF model has also been evaluated under different initial and boundary forcing conditions. Three new generation reanalyses (ERA-Interim, NASA-MERRA and NCEP-CFSR), an older reanalyses (NCEP-R2), and two analysis commonly used for wind energy (NCEP-GFS and NCEP-FNL) have been used as initial or bounding conditions for WRF. In this case, the best estimates of local potential wind energy production are obtained when the initial and boundary conditions are provided by ERA-Interim [22]. A very similar study has been conducted onshore around the Iberian Peninsula, and the WRF simulations driven with ERA-Interim also recorded lower errors when measurements are compared [23].

In all these previous studies, the WRF model has been run without using data assimilation. The current study is a follow-up to a previous work by this research team in which WRF with data assimilation (WRFDA) was used to evaluate offshore wind energy potential at the southern coast of the Bay of Biscay [30]. The results indicated a significant improvement in the assessment of this potential when data assimilation is used with WRF, thus pointing out that in this area previous evaluations of the wind energy resources were overestimated. This highlights the need to elucidate if these improvements in accuracy regarding wind energy potential evaluation are general or were only associated to the particular conditions of the Bay of Biscay. It is therefore of considerable interest to revisit the topic using a similar approach, but to a completely different area. This study has therefore chosen the Iberian Mediterranean coast and Balearic Islands. More specifically, this study covers a rectangular area to the east of the Iberian Peninsula and Balearic Islands (Figure 1). Cabo Begur (the cape on the left of point 6) is a key maritime marker. It is the most northerly cape on the Eastern Iberian Peninsula and signals the boundary between France and Spain. It opens onto the Gulf of Lion, whose high offshore potential is well-known in wind energy industry [31]. This point is the northern limit of our study area, which follows the Spanish coastline to another cape: Cabo de Palos (point 3). The Balearic Islands are in the middle of the study area, with an autonomous power supply grid within the Spanish electrical system.

The aim here is to make an accurate evaluation of the resource using a similar methodology as in [30]. A full-featured state-of-the-art 3DVAR data assimilation approach will be followed using a recent review of the WRF and WRFDA models. The main differences between this new simulation and the one in the previous paper can be summarized as follows. First, the WRF simulations will be nested in ERAI instead of in ERA40. Second, the SST data used in this dataset corresponds to the NOAA High Resolution OI blended analysis of daily SST and ice (0.25 x 0.25 degree resolution) [32]. Third, the current version of the simulation includes the NOAH land surface model instead of a diffusive model, an important aspect in Mediterranean areas [33]. Finally, a higher number of vertical levels is included in this simulation, thus yielding a better resolution of the Planetary Boundary Layer.

Wind potential depends not only on meteorology but also on legal criteria, such as the distance from the coastline, or economic and technical criteria, such as water depth

[10]. These aspects have also been taken into account in our research to calculate different approximate scenarios of wind energy resource assessment.

The paper is structured as follows. Section 2 describes the data used for the simulations and the verification of simulation and reanalysis with observations. Section 3 presents the main results of the paper. Section 4 discusses the results and paper finishes with conclusions and future outlook in section 5.

2. Data and Methodology

2.1. Data

This study has been conducted in the period running from 01/01/2009 to 01/01/2015 . The data used have been obtained from different sources:

- ERAI data [34] for the same area and period as downloaded from the ECMWF. These data were used to nest the two integrations of WRF called N and D, as well as for a comparison purposes (see below).
- Wind speed (module+direction) at a height of three meters above the sea level, and sea-state data from the six buoys operated by the Spanish State Ports Authority (Puertos del Estado) [35]. In Table 1 it can be seen the position, bathymetry and distance from the buoys to the ERAI gridpoints, and the two WRF integrations.

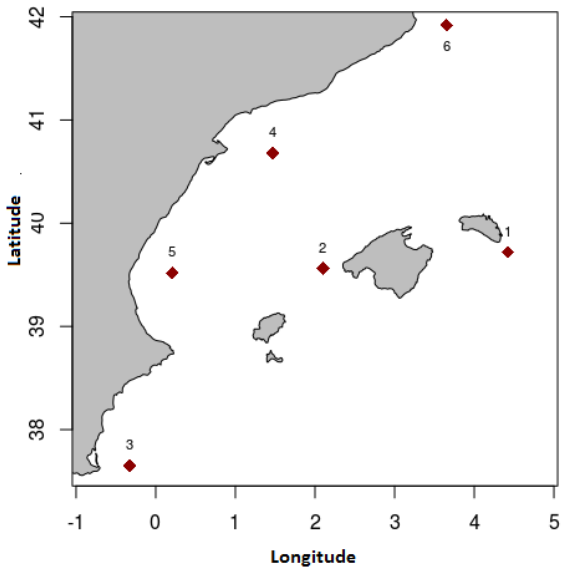

Figure 1: The area of study and the buoys used

Table 2: Properties of the buoys and stations

Id.	Name	Lon.	Lat.	Depth (m)	Dist.(km) N-D / ERAI
1	Mahon	4.42	39.72	300	8.8 / 7.6
2	Dragonera	2.10	39.56	135	8.9 / 24.7
3	Cabo de Palos	-0.3	37.65	230	6.7 / 33.5
4	Tarragona	1.47	40.68	688	6.7 / 20.2
5	Valencia	0.21	39.52	260	3.9 / 31.2
6	Cabo Begur	3.65	41.92	1200	3.7 / 12.1

- Being the objective to evaluate the performance of both WRF integrations, buoys do not provide spatial verification, they only allow a preliminary evaluation most of the times near the coast. So the second version of Cross-Calibrated Multi-Platform (CCMPv2) has been used for a full spatially-distributed evaluation of WRF outputs [36]. CCMPv2 processing combines Version-7 RSS radiometer wind speeds, QuikSCAT and ASCAT scatterometer wind vectors, moored buoy wind data, and ERAI wind fields, first using a Variational Analysis Method (VAM) to produce 6-hourly maps of 0.25 degree grid. Different datasets are distributed to complete the series, and we have used fully assimilated wind field data (L3.0).

- Finally, we have used NOAA's global relief model ETOPO1 [37] with one-minute resolution for the bathymetric study to calculate classified scenarios of annual energy production depending on water depth.

2.2. Methodology

2.2.1. WRF simulations

The two WRF simulations used here have involved WRF and WRFDA version 3.6.1 [38] and are denominated in this paper as N (without data assimilation) and D (with data assimilation). Figure 2 shows the domain where the model has been run (mass points are shown with red circles) and the studied area is marked by a blue rectangle. The domain is quite large, and so, as gathered by the literature for similar cases [39, 40], the results are not expected to be affected by border effects. The model has been run with a horizontal resolution of 15 km x 15 km and 51 vertical η levels up to 20 hPa.

The boundary condition data for both N and D runs have been downloaded from the MARS archive at the ECMWF with a 0.75 x 0.75 degree horizontal resolution and 22 vertical levels up to 5 hPa. ERAI fields are used as boundary conditions every six hours (00Z, 06Z, 12Z and 18Z). Two different WRF simulations covering the period 01/01/2009 to 01/01/2015 have been prepared. They use the same set of physical parametrizations and horizontal/vertical resolutions, with the only difference being the use (or lack of) 3DVAR data assimilation every time the WRF model is initialized at 00 UTC, 06 UTC, 12 UTC and 18 UTC. Since the NOAH land surface model is being used, the first year of the simulation (2009) is run for a proper initialization of the soil in the model, but those results are not

evaluated here, since they are only used as a spin up period for the soil model. Therefore, only the period 2010/2014 is compared with the observations.

The parameterizations used for both N and D experiments are the same: five class microphysics WSM5, RRTMG (longwave and shortwave) radiation with seasonally varying aerosols, and latitudinally, vertically and seasonally varying ozone data, Mellor-Yamada Nakanishi and Niino Level 2.5 PBL, revised MM5 surface layer scheme and Tiedtke cumulus parameterization. The NOAH land surface scheme is used. SST and ice are daily updated daily from the NOAA OI SST V2 High Resolution Dataset [41].

The first WRF-based experiment (N) does not use data assimilation, being fed by the boundaries every six hours. No grid nudging has been used in N outside the lateral relaxation zone. The D simulation is the same to the N experiment, except that a 3DVAR data assimilation step is run using WRFDA at 00 UTC, 06 UTC, 12 UTC and 18 UTC. This means that the initial conditions of the runs are prepared every six hours (06hDA), also considering observations corresponding to that time, and not only the state of the model at that time (the so called background). The model is therefore being corrected (every six hours) according to all the observations available at that time. Instead of using grid nudging [21], we are using a full 3DVAR variational algorithm in this case, so the background and observational errors are fully accounted for [42, 43].

In order to assimilate observations, use is made of PREPBUFR data from the NCEP ADP Global Upper Air and Surface Weather Observations dataset (ds337.0 in NCAR/UCAR's Research Data Archive). Observations are considered for assimilation when they are included inside a 120 minute window centered at every analysis time.

Special background error covariances have been produced for the data assimilation runs, being adapted to the domain and set of parametrizations used in this configuration of the model by means of the CV5 method [42, 44]. To do so, a special integration has been run for thirteen months, starting on 01/01/2007. The background error covariances vary monthly and are generated from 90 days of this special integration (runs initialized at $00Z$ and $12Z$). Runs from January, February and March are used to create the background error covariance used during February, and so on. For other options of WRFDA, such as thinning and observation minus background checks, WRFDA's default values are used. Three external cycles are performed during the analysis.

WRF outputs have been saved every three hours (00 UTC, 03 UTC, 06 UTC, 09 UTC, 12 UTC, 15 UTC, 18 UTC and 21 UTC). The values at 00 UTC, 06 UTC, 12 UTC and 18 UTC correspond to analyses, whilst the values saved by the model at 03 UTC, 09 UTC, 15 UTC and 21 UTC correspond to forecasts three hours ahead from analyses.

During the post-processing stage, and in order to estimate the wind energy potential at hub height, wind speed, pressure and virtual temperature for the air density, at 70 m, 130 m and 180 m have been computed, interpolated from model results for the original model grid in η coordinates.

2.2.2. Evaluation of WRF runs

The wind field outputs at 10 m.a.s.l. at almost 2500 gridpoints cover the area corresponding to the two WRF simulations, N and D, every six hours, the ones corresponding to

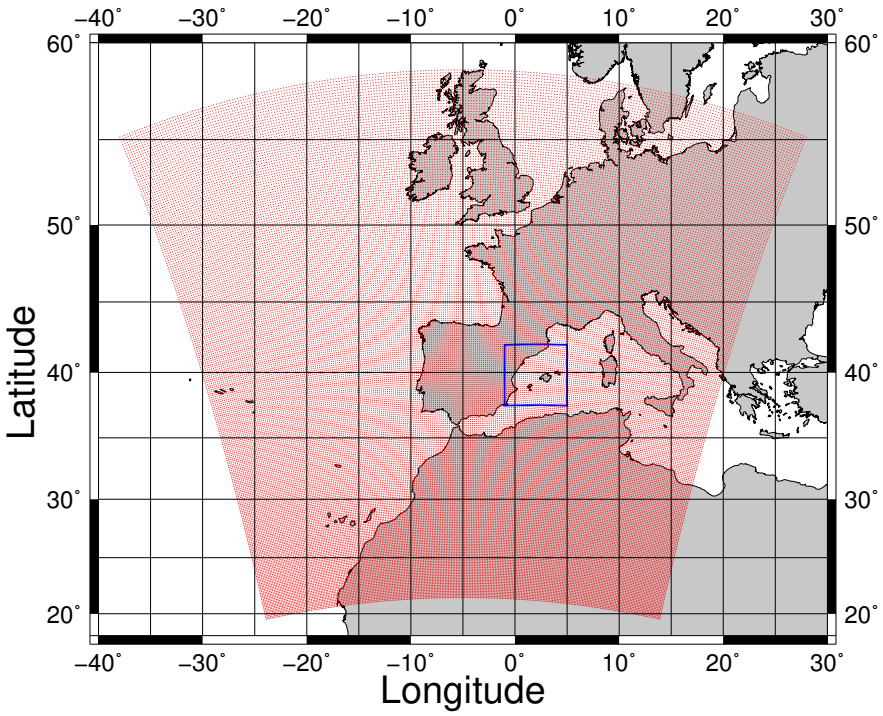

Figure 2: Above: WRF simulation domain; Blue rectangle: area of study

ERAI, have been evaluated against observations at the nearest gridpoints from two different sets of observations: six buoys and the above mentioned gridded multiplatform satellite analysis, CCMPv2 data. The evaluated period runs from 2010 to 2014. Additionally, ERAI wind data have also been used for reference purposes.

The statistical indicators used for that evaluation have been the correlation coefficient (r), the root mean square error (RMSE) and the standard deviation ratio (SD ratio). **These indicators and the mathematical relations between them are defined in [45]. We have also used the mean average error (MAE) for the six buoys defining the average error at each buoy as**

$$AE = \mid \frac{\overline{U}_{mod} - \overline{U}_{obs}}{\overline{U}_{obs}} \mid \tag{1}$$

where $\overline{U}_{mod}$ and $\overline{U}_{obs}$ are respectively the mean wind speed given by the model and the mean wind speed given by the buoy's observation. Thus, for our six buoys indexed by n, $MAE = \sum_{n=1}^{n=6} AE_n/6$, being AE_n the average error at the n buoy.

In all cases, the differences in performance according to this set of indicators have been assessed at a 95% confidence level using bootstrap resampling with 1000 samples. A preliminary stage of data preprocessing was carried out to arrange the data from all the sources along the same time line. A total of 7304 cases were used.

The WRF runs were evaluated in two steps. The first step was to check N, D, ERAI

and CCMPv2 wind speed data against buoy data at the nearest gridpoints corresponding to the WRF grids [35]. All the buoys have their anemometer at a height of 3 m ($z = 3m$), and it was necessary to estimate wind speed at 10 meters to compare with the two WRF simulations. Instead of assuming a constant roughness [23], Hsu's [46] equation was used to calculate the instantaneous roughness of the sea (z_0):

$$\frac{z_0}{H_s} = 1200 \left(\frac{H_s}{L_p} \right)^{4.5} \tag{2}$$

where H_s is the significant wave height, and L_p is the peak period wavelength, which are obtained from each buoy's dataset together with wind speed data. Roughness was used to apply the logarithmic law of vertical wind shear that can be also used for low heights (bellow 10 m) [47] :

$$\frac{U(z)}{U(z_r)} = \frac{\log((z + z_0)/z_0)}{\log((z_r + z_0)/z_0)} \tag{3}$$

obtaining an estimation of wind speed at 10 m, $U(z = 10)$, in terms of the speed of reference, $U(z_r = 3)$. After establishing the same height for the model and buoy wind speed data, correlation and RMSE were used to plot Taylor Diagrams [45]. The points in this plots that represent N, D, ERAI and CCMPv2 are expanded in a cloud of points according to the correlation and RMSE computed by means of bootstrap resampling. We thus know whether the separation between the two runs and ERAI is significant compared with the difference between two different observational datasets, buoys and CCMPv2 purportedly.

Second, buoy data were only available at six locations, so N, D, and ERAI have been evaluated versus CCMPv2 to provide a comprehensive evaluation of the WRF runs in spatial terms over the study area in comparison to the reference ERAI spatial distribution. The correlation, RMSE and SD ratio have been calculated over all the points of the study area at their nearest gridpoints, together with their 95% confidence intervals between CCMPv2 and the three datasets.

2.2.3. Wind Energy and Capacity Factor Calculation

After validating the two WRF simulations, outputs corresponding to the best run have been used to calculate the annual energy production for three types of different turbines:

1. A low turbine: 2.4 MW wind turbines of 92 m diameter (MWT-92/2.4 by Mitsubishi Heavy Industry), and with the hub at 70 meters [10, p. 511]. From the original η levels in the model, the wind speed, pressure and vitual temperature (therefore density), have been vertically interpolated to the hub level. We will use it as reference for the depiction of the Capacity Factor (CF) colour maps over the study area.
2. A higher turbine, such as Siemens 2.3 MW of 90 m diameter (Siemens-90/2.3), with the hub at 130 meters above sea level, like the turbines tested in Stavanger (Norway) for the first floating wind farm in the world: HyWind Scotland by Statoil [2].
3. Following this completed test, the Hywind-type wind farm turbines located in Scottish waters will be 6 MW and with the hub at 178 m. We will also estimate and discuss

the energy production for the implementation of these turbines in the selected areas (Siemens-160/6.0).

An important advantage of our study is that the pressure, temperature and wind values from WRF simulations have been directly interpolated from the original η-levels to hub height. The logarithmic wind shear is only used for verification at 10 meters, as the productive wind speed at the hub is obtained directly from model's outputs.

A normalized wind speed has been calculated to incorporate the influence of air density into the wind power equation. As power is proportional both to density, and to the cube of wind speed, we have used the temperature and pressure of the simulations to obtain the density ρ of the air at hub height, with the normalized wind speed U_n therefore being:

$$U_n = U \left(\frac{\rho}{\rho_0} \right)^3 \tag{4}$$

where ρ_0 is standard air density ($1.225 kg/m^3$).

According to [48], the Capacity Factor (CF) of a commercial turbine depends on the average wind speed $\overline{U}$ in m/s, the rated power P_R in kW, and the diameter D in meters:

$$CF = 0.087 \overline{U}_n - \frac{P_R}{D^2} \tag{5}$$

Therefore, CF has been calculated in terms of the average wind speed in our 5-year period of analysis (2010-2014). Finally, CF provides the turbine's annual production:

$$E_a(TWh/year) = CF \cdot P_R \cdot 365.25 \cdot 24 \cdot 10^{-12} \tag{6}$$

2.2.4. Distribution of the wind farm

Another major consideration is the spatial distribution of the offshore wind farms. The spatial separations between wind turbines are assumed to be eight times the rotor diameter (8D) parallel to the predominant wind direction and five times D (5D) perpendicular to it, because the representation of buoys' wind roses (Figure 6) have shown that the north-south line is much more prevalent than the perpendicular east-west line. With this interval, the influence of the wake can be ignored. So, if the intervals between two turbines in west-east and south-north directions are respectively 8D (736 meters) and 5D (460 meters), the number of turbines per km^2 would be approximately $1/(0.736 * 0.460) = 2.953$ in a wide enough area. This factor enables us to calculate the maximum number of turbines deployed in a certain region at sea delimited by isobaths or by other kinds of restrictions.

The final step is to assign a CF to each turbine. To do so, we have calculated the CF at each WRF gridpoint for the three turbines over the study area (Equation 5), and we have considered a square area of influence centered on the gridpoints (see Figure 3). The turbines inside a square area of influence (shaded pink) have the same CF corresponding to the corresponding WRF wind speed data in each one of the simulations. On the left, the map shows an amplified view of the two areas selected for their high wind energy potential. The potential of these sites will be shown finally in the CF colour maps.

2.2.5. Bathymetry and legal and technical constraints

Finally, there are two important constraints on the placement of turbines in the areas shown in Figure 3: a legal one and a technical one. A 10 km blue buffer has been drawn parallel to the coast as a prohibited area because the European Commission [49] considers it as a protected coastal area. Another important concern is bathymetry, as the technical literature usually considers it impossible to properly anchor floating wind turbines in water deeper than 1000 meters [50]. The isobaths calculated from the ETOPO1 dataset [37] are depicted in red color in order to obtain a classified energy production depending on depth intervals of 200 meters.

Figure 3 shows that the bathymetry reaches a depth of 1000 m at a distance of less than 100 km from the shore, except for a small region on the south of Gulf of Lion, and there are now operational AC sub-sea cables that run up to 120 km. Additionally, HVDC technology's direct electrical transmission will remove practical distance limits in the future [51]. Therefore, in the case of the Iberian Mediterranean coast and Balearic Islands, bathymetry alone conditions the upper range limit for offshore floating wind farms, as the distance from the coast has no influence in this case, with this being the main constraint of broad, shallow continental shelves.

To summarize, the following methodological steps have been taken:

1. An initial verification of the two WRF runs and ERAI against three buoys near the coast.
2. A full evaluation at the gridpoints of the area of study used for N, D and ERAI at the nearest corresponding CCMPv2 gridpoints.
3. Identification of the most accurate WRF run.
4. Identification of areas with high potential for the implementation of an offshore wind energy farm.
5. In these locations, the estimation of wind energy potential according to the best run. We consider technical and legal aspects, and the classification of floating wind turbine positions and outputs according to different bathymetric scenarios.
6. Finally, technical and production differences are also estimated for farms with the three turbines mentioned, namely, MWT-92/2.4, Siemes-90/2.3, and Siemens-160/6.0.

3. Results

3.1. Verification versus buoys and CCMPv2 analysis

Figure 4 checks N, D, CCMPv2 and ERAI wind data against the six buoys compared. For CCMPv2, ERAI and D the RMSE is similar at the six buoys, between 2 and 3 m/s. The correlation coefficient, however, seems to be locally dependent, with values for Mahon, Cabo de Palos and Cabo Begur around 0.8, Dragonera and Tarragona around 0.7 and Valencia Copa around 0.6 .

Figure 5 reveals a fairly similar performance for CCMPv2, ERAI and D, whose results tend to cluster together, and clearly outperform the N integration. As CCMPv2 is also

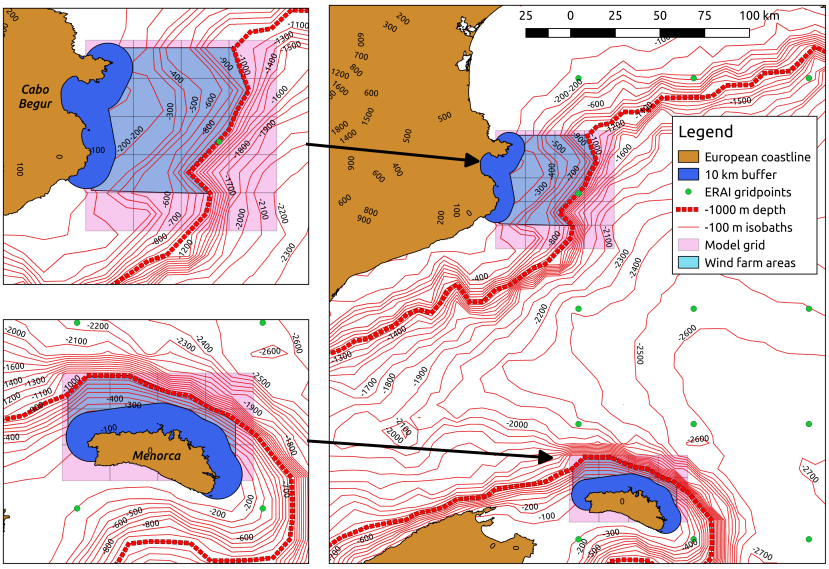

Figure 3: Detailed map of the area of study with all the restrictions

derived from observational data, its inconsistencies with the different buoys also represents an inherent error between two observational sources. The fact that both ERAI and D are close to CCMPv2's error suggests that current ERAI reanalysis and our D simulation show an error against in-situ observations that are very similar with the one produced by an alternative state-of-the-art observational gridded dataset. The error therefore seems to be very close to the limit of the observational error.

A more detailed comparison shows that in all cases CCMPv2 records slightly closer similarities with buoys observations. This is to be expected, as CCMPv2 data are also observational. However, it is more interesting to compare ERAI to N and D WRF integrations. The reason is that any computational simulation effort with WRF is expected to yield better results than the plain use of ERAI, which is used to feed the N and D integrations. Additionally, with similar indicators of general performance a further advantage is that WRF integrations can provide a higher spatial resolution than ERAI.

The results show that in all cases N records a higher RMSE and a lower correlation coefficient than ERAI and D. Considering the cloud of points at a 95% confidence level, a comparison between ERAI and D indicates that at Cabo de Palos, ERAI and D perform equally from all points of view. At three buoys (Tarragona, Valencia Copa and Cabo Begur), ERAI and D also record similar values of both the correlation and RMSE. Regarding the the buoys of Mahon and Dragonera, D records slightly lower values of the correlation coefficient and higher values of the RMSE. However, in five buoys out of six, D is significantly closer than ERAI to the arch corresponding to standard deviation (SD) ratio of value 1. ERAI and D have very similar correlation coefficients at all the buoys, which means that the improvement in D integration with respect to ERAI is its ability to better capture and describe oscillations due to breezes, for example, and mean-high observational values. In

the particular case of Cabo Begur, with the highest recorded wind speed, D has a SD ratio higher and closer to 1 than both CCMPv2 and ERAI. With similar values of the correlation coefficient, this means that D is able to better capture high speed values. In any case, as mentioned above, the differences between ERAI, D and CCMPv2 are not overwhelming thus indicating that ERAI and D are close to the observational error inherent to the differences between two observational datasets (in-situ buoys and gridded CCMPv2).

It is important to note that the simulation without data assimilation (N) clearly gives higher errors than with data assimilation (D). The distances to the nearest gridpoints for all the experiments can be seen in Table 1, and they do not appear to have an important effect on performance.

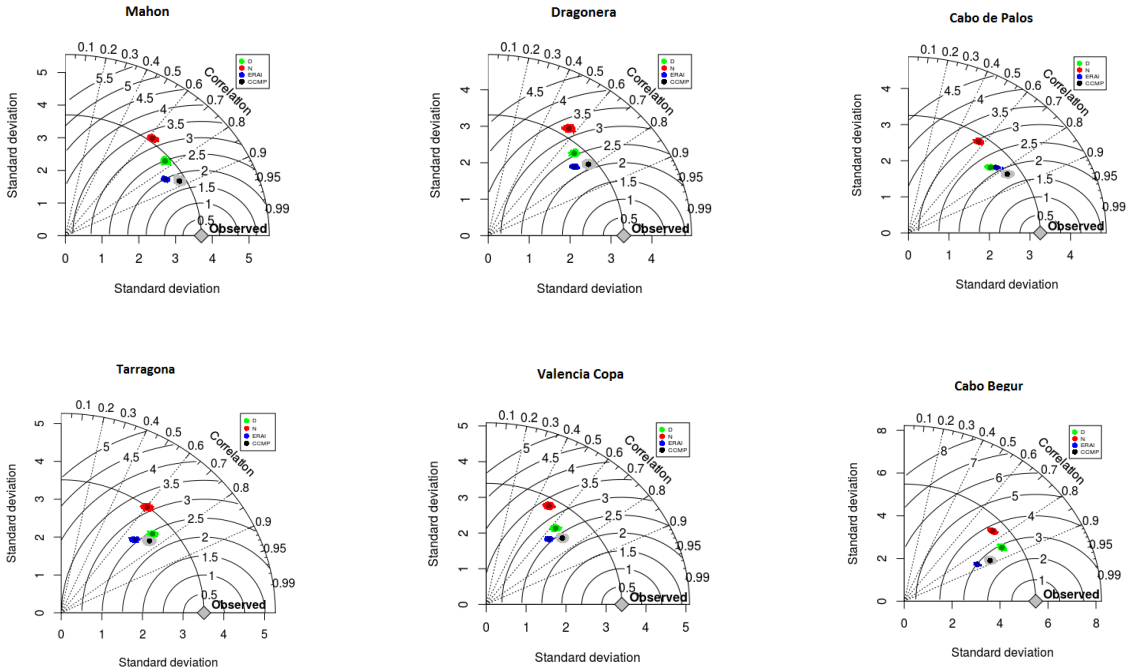

Figure 4: Taylor diagrams at the six buoys

Next, our two simulations (N and D) and ERAI have been spatially compared at their nearest gridpoint to the CCMPv2 surface wind analysis. Figure 5 shows N, D and ERAI plotted against CCMPv2 correlation, RMSE and SD ratio colour maps. The same colour bar is used for the three indicators in order to compare them via the same scale (between 0 and 4 m/s for RMSE, between 0 and 1 for correlation, and between 0 and 2 for SD ratio). Furthermore, the colours of the values obtained for the three indicators with the buoys are added in their positions with a diamond-shaped symbol.

The CCMPv2 has been taken as a reference since it is derived mainly from observations. The SD ratio, RMSE and the correlation between buoy observations have been considered as benchmarks for providing a ranking of models.

The comparison has involved the following steps:

Table 3: Difference of the statistical indicators around the buoys. The best case and worst case are shown and also the corresponding buoys.

Indicators	ERAI vs. Buoy-CCMPv2	D vs. Buoy-CCMPv2
Correlation	Valencia, 0.55 - CaboBegur, 0.05	Valencia, 0.15 - Tarragona, 0.05
RMSE (m/s)	Valencia, 3.2 - CaboBegur, 2.1	CaboBegur, 0.9 - Mahon, 0.4
SD ratio	CaboBegur, 0.7 - Mahon, 0.4	CaboBegur, 0.4 - Dragonera, 0.2

1. Regarding the models considered (ERAI, D and N), calculate the correlation coefficient, SD ratio and RMSE with CCMPv2 observations at the nearest gridpoints from the buoys.
2. Regarding the models considered (ERAI, D and N), calculate the correlation coefficient, SD ratio and RMSE with buoy observations (diamond-shaped symbols).
3. The comparison made using the three indicators mentioned above will show whether ERAI, D or N tend to over/underestimate model's performance at the buoys. This information will be used in the following step to correctly evaluate results under the assumption that any systematic over/underestimation behavior detected at the buoys can be applied to the whole area.
4. The three indicators for ERAI, D and N with the closest CCMPv2 observations will be calculated for all the gridpoints in the area.

The analysis clearly shows that the N integration has by far the worst performance. The results indicate that the highest correlations and smallest errors at the gridpoints are observed with ERAI. However, a comparison with buoy observational data (diamonds) shows important discrepancies in results around those locations, thus suggesting that ERAI tends to overestimate performance, perhaps because CCMPv2 has already assimilated ERAI data, as ERAI is used as background by CCMPv2 in its variational. However, the D integration has a much closer agreement between correlations, RMSE and SD ratio with both CCMPv2 and buoys.

The Table 3 shows the best and the worst case (highest and lowest difference) for each statistical indicator in the locations of the buoys, presenting the absolute difference of the statistical validation against the Buoy and against CCMPv2 and the corresponding location where the difference is computed. The differences showed by the D simulation are much lower than the differences of ERAI in every case. For example, we should mention the hight differences of ERAI over the Valencia buoy compared with D's worst case, which are less than a third for correlation and RMSE.

This means the indicators corresponding to the D integration throughout the whole area are more reliable. Besides, the D integration has a higher spatial resolution (15km, five times better), thereby allowing a better fit in irregular coastal regions.

The correlations increase is step with the distance from the coastline, and as the gridpoints approach the open Mediterranean towards the south-east, out of the area between the Balearic Islands and the north-eastern Iberian coast. The improvement in D over N is

significant, and its correlation map is as good as ERAI, although, as mentioned, with an important increase in the spatial density of the gridpoints.

On the other hand, the spatial distribution of RMSE does not follow a clear spatial pattern, and it does not seem to be directly related to the distance from the coast. D's RMSE spatial distribution is not as good as ERAI's one: generally speaking, D is around 2.5 m/s, while ERAI is around 1.5 m/s. Nevertheless, we should not forget that CCMPv2 is built with a variational analysis that uses ERAI winds as the first-guess field. Again, the colour differences between diamonds and the colour around them on ERAI maps clearly reflect this aspect. Buoys record higher RMSE values than the ones corresponding to the CCMPv2 blue background. These values for the buoys are closer to the ones in the D experiment. These colour differences are much weaker for N and D in the three indicators. This again indicates that an evaluation of ERAI performance adopting CCMPv2 as a reference leads to an overestimation of its performance, and is not as reliable as D.

Given these important findings, it may be said that D's validation results are of good quality, and that it provides wind data with a much higher spatial resolution than ERAI, so it better estimates the wind energy resource and its spatial variability.

Finally, as the main variable of our estimation method is mean wind speed, we have also calculated the mean values of all the sources over the position of the buoys or the gridpoints nearest the buoys. For the mean speed at the six buoys the mean average error (MAE) is 5.7% for D, 6.8% for ERAI, and 24.3% for N. This again indicates a slight improvement, that is, a smaller bias, of D over ERAI, with a MAE roughly four times smaller than N.

The 2010-2014 period has been used in every case. Ten sources (six buoys, one gridded analysis, our two models and ERAI) have been evaluated. The results indicate that the improvement from N to D is very clear. However, the better standard ratio of D over ERAI observed in the buoys for roughly the same correlation coefficient and the higher spatial resolution provided by the WRF D integration indicate that a more accurate assessment of the wind resource is obtained for the area using the D run. Additionally, the better agreement of D in the area around the buoys suggests that the results for D are more reliable than for ERAI.

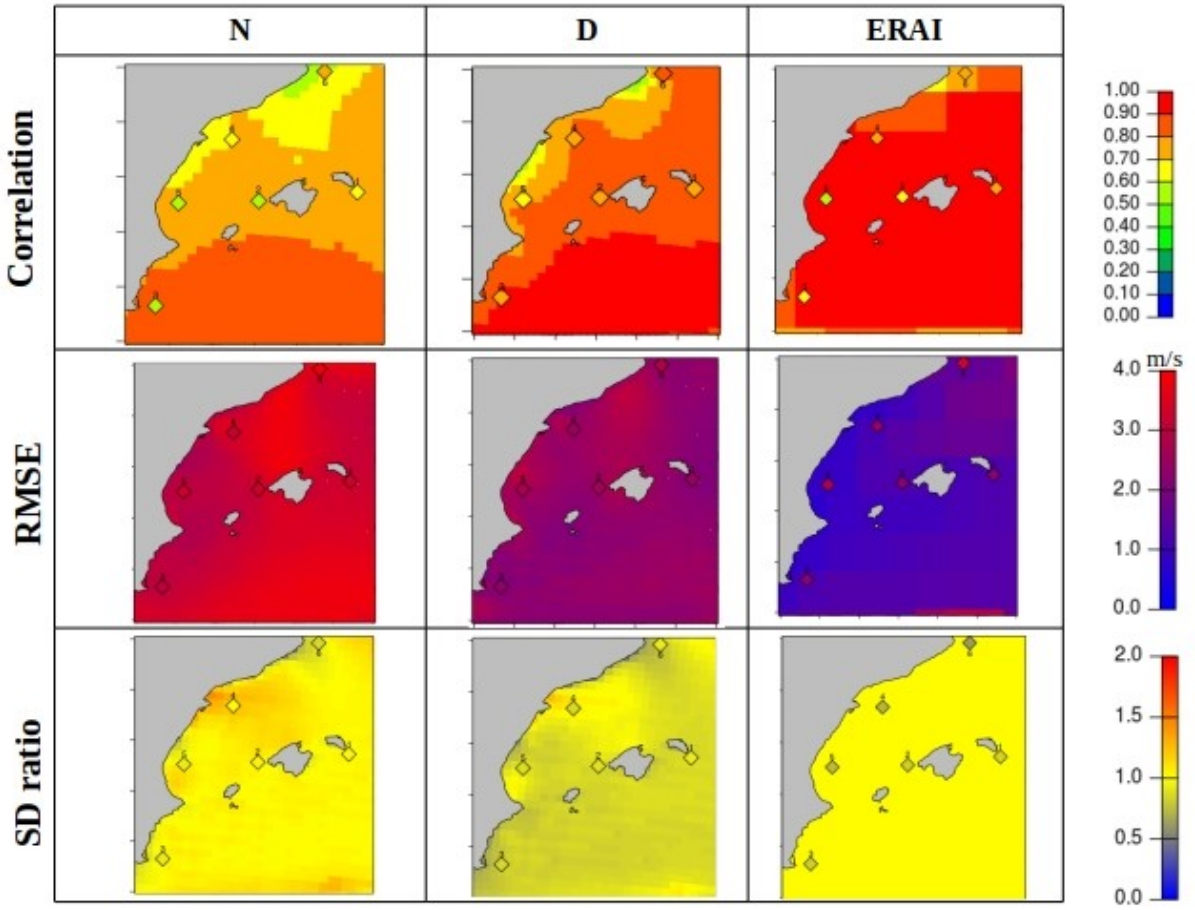

Figure 5: Correlation, RMSE and SD ratio maps of N and D experiments and ERAI versus CCMPv2

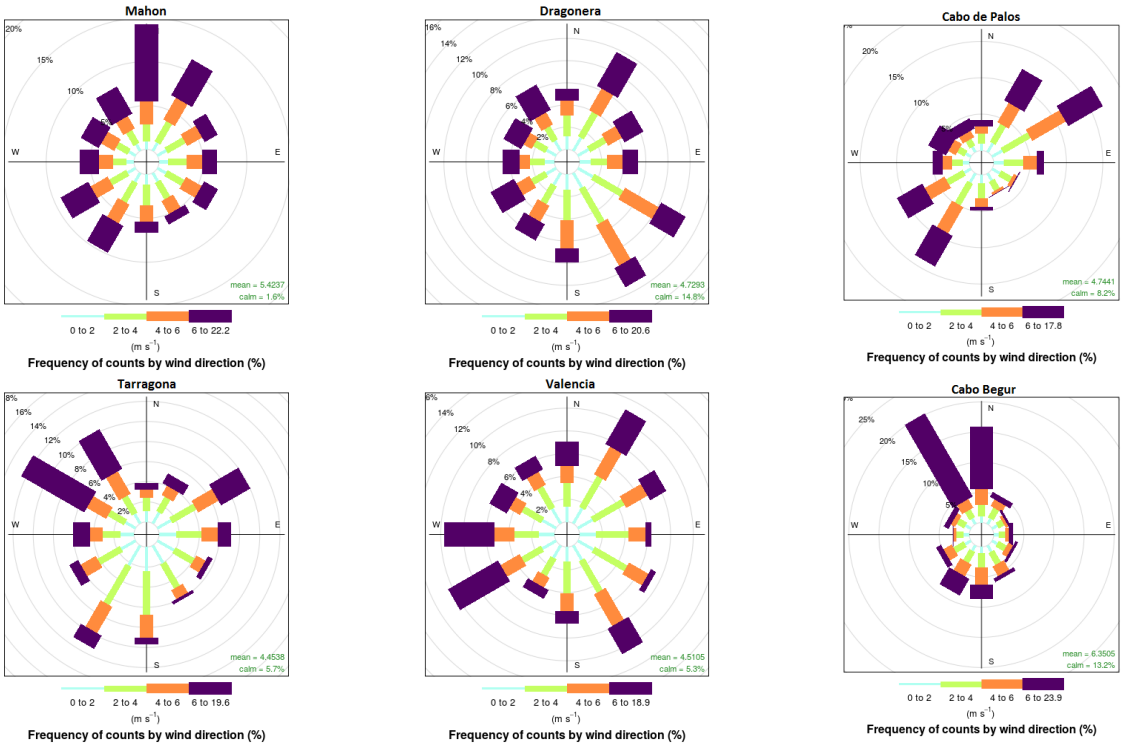

Figure 6: Wind Roses at the six buoys

3.2. Annual wind energy potential

Evaluating the wind energy potential at a given location requires knowing its wind rose. Here we also present the wind rose of each buoy, with major differences in the prevailing wind direction, with strong winds from the north compared to east-westerly ones (Figure 6). This general wind rose configuration establishes the distribution of the wind farm with a separation between turbines of 8D along north-south line and 5D in an east-west direction.

The values of Capacity Factors have been obtained at all the WRF gridpoints by using Equation 5 and model wind speed and density data. In this case we show the results for the MWT-92/2.4 turbine at a height of 70 m; that is, the wind speed at hub height directly given by the two simulations, and so we do not need a vertical approximation by means of the logarithmic wind shear, as in other similar studies. The results for the two simulations and ERAI over our study area can be seen in the annual and seasonal colour maps in Figure 7. As is to be expected from the previous results, the CF improves towards the south-east or to the north-east, that is, moving away from the shore and approaching the open sea away from the archipelago or entering the the Gulf of Lion. An important aspect of the comparison between N and D simulations is the lower CFs predicted by the D dataset with data assimilation and its greater similarity with all ERAI maps, annual or seasonal. The three colour maps show a clear overall reduction in the CF from the N simulation to D one, for all the annual and seasonal maps. Thus, the most accurate wind energy estimation is the most conservative one. In every case, winter is the most energetic season, followed by autumn, spring and, finally, summer. This result can be expected, given that strong northern Tramontana winds are an important local meteorological phenomenon in winter. According to the most reliable D run, the maximum annual CF is located in front of Cabo Begur, and it is as high as 49%, rising to 60% in winter; this is the first selected area with high wind potential. The average annual CF in the whole study area is 37%, but as pointed out above, with a strong seasonal variation.

The minimum CF values are very low, and can be located on the gulfs along the Iberian coastline protected from northerly winds, so the second selected coastal area with high potential is the north of Menorca, where there is no such protection against the strong northerly winds (see Dragonera wind rose), with an annual CF of 32% (44% in winter) according to D simulation.

Table 4 summarizes all the results obtained for the estimation of annual wind energy production in the selected Cabo Begur area (3). The table shows the number of turbines for MWT-92/2.4 (times $92^2/90^2 = 1.04$ for Siemens-90/2.3 and $92^2/160^2 = 0.33$ for Siemens-160/6.0) and their energy production classified at 200 m depth intervals for our three turbines at their hub heights (at 70 m the MWT-92/2.4, at 130 m the Siemens-90/2.3, and at 180 m the Siemens-160/6.0) according to the best D simulation. We estimate that a total number of 6840 turbines over an area of 2318 km^2 with a installed capacity of around 16.4 GW for the three turbines (see Section 4), could produce 55.8 TWh in the most reliable D case at 70 m and approximately 13% and 18% more for Siemes-90/2.3 and Siemens-160/6.0. Furthermore, most of the turbines would be installed over shallower bathymetric intervals.

Table 5 shows the same variables for the second selected area, north of Menorca. Here, although the selected zone is similar, the real available area is smaller because of the steep

Table 4: AEP (TWh) for the three models over the area of Cabo Begur

Intervals (m)	N. turbines	at 70 m	at 130 m	at 180 m
0-200	1190	9.71	10.96	11.45
200-400	1790	14.31	16.17	16.88
400-600	1980	16.12	18.21	19.02
600-800	920	7.53	8.50	8.88
800-1000	960	8.11	9.16	9.56
Total	6840	55.78	63.03	65.82

Table 5: AEP (TWh) for the three models over the area north of Menorca

Intervals (m)	N. turbines	at 70 m	at 130 m	at 180 m
0-200	0	0.0	0.0	0.0
200-400	140	0.72	0.81	0.85
400-600	510	2.68	3.02	3.16
600-800	550	2.85	3.22	3.35
800-1000	500	2.54	2.85	2.99
Total	1700	8.79	9.93	10.36

bathymetry, and only 1700 turbines fit within the area of 576 km^2, with a total installed capacity of 4 GW for MWT-92/2.4. Additionally, most of the turbines would be over the deepest bathymetric intervals (400-600, 600-800, 800-1000). However, the distances of the turbines to the coastline are much shorter.

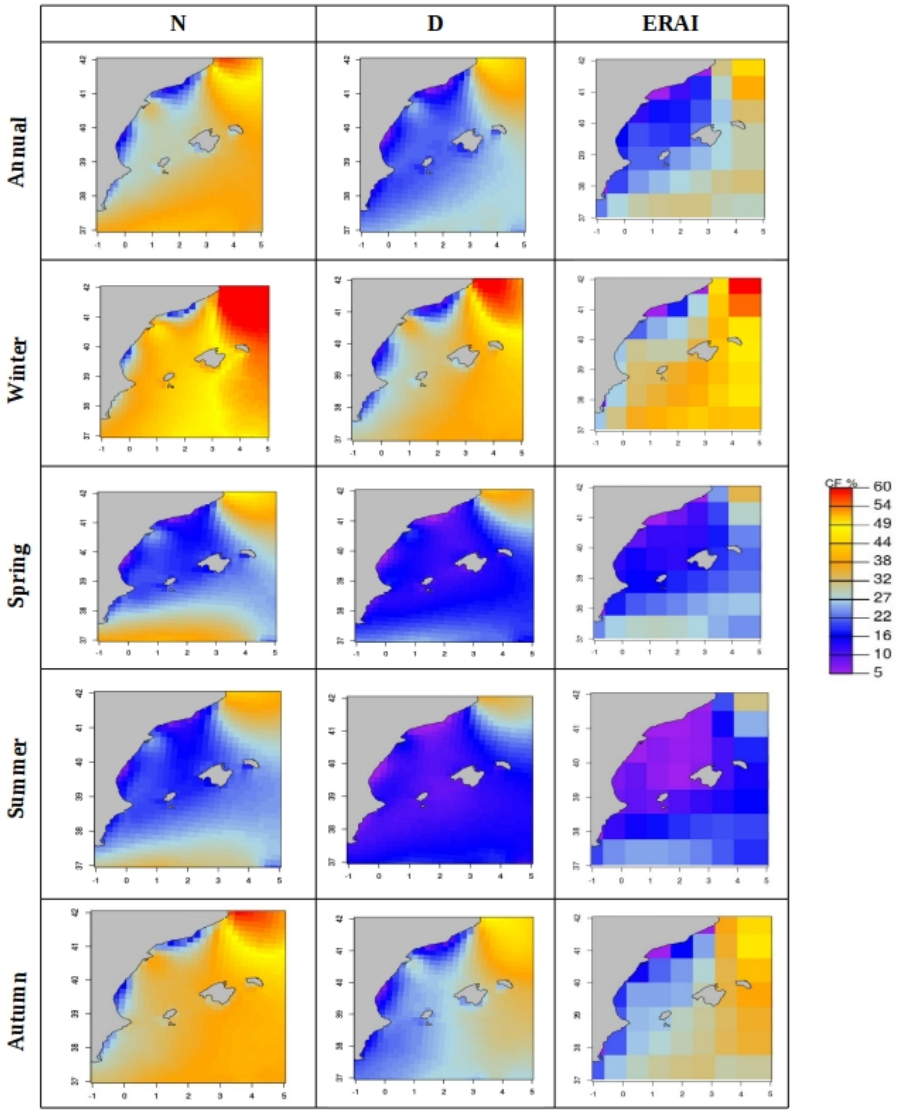

Figure 7: Annual and seasonal capacity factor maps

4. Discussion

An analisys of the sensitivity of the CFs to the use of 3DVAR data assimilation in WRF simulations in WRF simulations is a logical continuation of previous works. As mentioned, Carvalho et al. recently showed for the Iberian Peninsula that ERAI should be considered the best reanalysis for nesting inside these results mesoscale wind simulations [18, 20, 21, 22, 23] with the NCEP-FNL and NCEP-GFS analysis being the best alternatives to ERAI [21]. Therefore, on this point concerning the use of ERAI as the best reanalysis that can be used to test a mesoscale model, we have revisited the sensitivity of the results in the estimation of potential offshore wind energy to the use of (or lack of) 3DVAR data assimilation every 6 hours in the D experiment (or no use of 3DVAR in the case of the N experiment). The results in this case , for a different area and using a new generation of the model, and different parametrizations (particularly the use of the NOAH land surface model) ratify our previous validation results [30].

However, apart from the use of data assimilation, we present four main novelties in our methodology, for the first time to the best of our knowledge, that can be applied in offshore wind energy estimation:

1. **From the η levels of our WRF simulations we have obtained wind speed outputs at three different heights for the estimation of wind energy potential in the selected areas. Furthermore, these heights correspond to real offshore wind turbines with their specific characteristics in diameter and rated power.**
2. Furthermore, we are using pressure and virtual temperature to normalize the wind speed at the turbine heights considering the contribution of the air density. We only know one work that uses a similar method [10], but they use an older generation of an atmospheric model. As we clarify in the next section 5, the air density can show important seasonal variations and our seasonal CF maps (Figure 7) contain this contribution that is often ignored.
3. **We have used the log law that determines the vertical profile only for the validation process and to bring the buoy's wind speed from 3 m to 10 m, but we should emphasize that the law used is specific for low heights and that the contribution of the roughness (z_0) in this equation (Eq. 3) is different compared to the classical equation used in our previous work.**
4. **Another novelty related to the previous one in our validation method is the computation of the instantaneous roughness of the sea according to the wavelength and wave period given by the buoy [46]. In this way we can obtain the wind speed at 10 m in a given instant, because the buoys provides wavelength, wave period and wind speed at 3 m in that instant.**

According to the results, the worst correlation is given by the Valencia buoy, protected within the gulf; in order from worst to best, it is followed by the two buoys of the Balearic islands, also protected between islands, and then the buoys more open to the sea: Tarragona, Cabo de Palos, and, finally, Cabo Begur. The behavior of RMSE is more complicated,

because the hight mean wind speed values in Cabo Begur produce higher absolute errors, with exactly the opposite occurring in case of weaker winds within the gulfs and between islands. If we assume that the observations from buoys are more realistic than CCMPv2 (a product that has undergone a post-processing stage), even after applying the Hsu equation to move from a height of 3 m to 10 m (Equation 2), the reliability of our results with data assimilation also increases near the shore. This and the 10-km legal exclusion zone from the shoreline indicate that even for the first possible lines of turbines over our two selected areas, using D is an improvement over N.

The improvement in the verification by D simulation stretches southward from the islands, and it increases below the cape Cabo de la Nao, where the models simulate the open sea without geographical barriers. This zone around Cabo de la Nao has not been considered as a potential area because of its steep bathymetry and the subsequent reduced area of possible implementation. Moreover, the CF is not still as important as in the other two cases, probably due to the geographical obstacle set by the proximity of the island of Ibiza in a north-easterly direction.

The areal potential estimations for the two selected regions (around 15-25 MWh/km^2) are quite similar to those obtained in other studies on offshore wind potential [10, 30]. The estimated installed capacities of 16.4 GW (Cabo Begur) and 4 GW (Menorca) consider the full use of the selected areas, ignoring major legal and operational restrictions. This installed capacity is on par with the projected growth in British offshore wind power. According to [1] and the UK government's strategic assessment, the installed capacity of offshore wind farms in that country could reach between 13 and 20 GW by 2020, starting from only 0.88 GW in 2009 [52].

In Cabo Begur's case, most of the turbines would be installed in shallow waters, with lower initial anchoring costs for the floating turbines. Menorca's case is different because the mooring costs may be higher due to the steeply sloping seabed. However, the turbines are close to shore, and this is good for the installation of the underwater power cable and for OM activities. According to [1, p. 133], this project would involve a large number of jobs in the future (700,000 in 2030). OM would create 0.48 jobs per installed MW; that is, if we consider only a spatial use of 10% for the selected areas, Menorca would create 190 jobs and Cabo Begur 930. Previously, prior installation and manufacturing would need 28.8 person years per MW; that is, 1150 jobs per year in Menorca and 5590 jobs in Cabo Begur, assuming ten year construction period. In addition, we should note that some studies have reported that offshore wind energy will be able to compete with oil between 2017 and 2033 (*ibid*).

The private sector and stake-holders may be attracted by these expectations for the near future, and by experiences such as those of El Hierro in the Canary Islands (Gorona del Viento, [53]), which have also set interesting energy precedents based on wind energy for the electrical supply of islands. In this sense, given its high potential, it would be interesting to study the orography and geology of Menorca for the installation of a hydro-wind power plant, as a clean energy alternative to the recent, and socially controversial, oilfield prospections [54], although other kinds of environmental concerns should be taken into account. Since the Balearic Islands have an independent electricity structure, monthly electrical demand data

are available for the islands [55]. The current annual demand is almost 6 TWh, slightly less than the AEP estimated for our best simulation of northern Menorca with full occupation of the area considered. In other words, a wind farm occupation of 10% of the area considered in Menorca would generate more than 10% of total demand on the Balearic Islands, together with the creation of all the aforementioned jobs. On the other hand, a wind farm with a full occupation of the Cabo Begur area would generate more than double the annual historical mean onshore wind energy generated in Spain (500 TWh in 20 years according to [56]).

Moreover, this is true for our referential turbine with a hub height at 70 m, but energy production would be even higher with taller turbines. We should first consider the turbine diameter variable for the wind farm's configuration: if the same hub height is used, any other study for these two areas considering larger wind turbines would give very similar overall energy production values. However, even though the energy captured per turbine would increase with D^2, the wake effect would require decreasing the number of turbines per unit area with D^{-2}. We should note that the change of the subtracted term P_R/D^2 in Equation 5 is almost negligible for the turbines mentioned above if we do not use large turbines: 0.284 for our reference MWT-92/2.4 turbine, exactly the same for Siemens-90/2.3, and 0.234 for Siemens-160/6.0. Therefore, the advantages are clear for the large turbine: this subtracted value is smaller and there are, obviously, taller hubs with higher mean wind speed, 178 m in this case. Considering these facts in detail and the wind data for the vertical levels of our D run (see the approximate relations in Tables 5 and 4, the AEP for wind farms constituted by Siemens-90/2.3 turbines (hub height at 130 m) would increase 13% with respect to our reference MWT-92/2.4 farm, and up to 18% for Siemens-160/6.0 farms (hub at 178 m).

In Menorca, the increase with Siemens-160/6.0 farms implies almost 1.5 TWh annually, and almost 10 TWh at Cabo Begur. Therefore, the increased production with higher hubs would be considerable for geometrically similar turbines, with no major loss in terms of placement, installation and maintenance, while reducing the number of turbines with the inverse of D^2. Finally, as a comparative term, our estimation for these turbines to be installed in the Hywind Scotland project establishes an approximately invariant potential with a mean annual areal production of $28.2 MWh/km^2$ over the available sea area in the most reliable case. This value based on advanced WRF simulations is an approximate reference for offshore wind energy, except for areas where local or large-scale jet streams in the upper atmosphere are important.

The mooring system generally informs the offshore wind turbine design, and it also needs to be discussed, as it is essential for cost evaluation. [5] compares the LCOE of five current state-of-the-art designs: Spar-Buoy (Hywind II), Tension-Leg-Spar (SWAY), Semi-Submersible (WindFloat), Tension-Leg-Wind-Turbine (TLWT) and Tension-Leg-Buoy (TLB). This study shows that larger wind farms are more viable: the cost decreases with the number of turbines of the farm and for more than 1000 turbines the LCOE records a constant value between 135-145 euro/MWh for the five designs. Therefore, both selected areas with thousands of turbines would be in this minimum asymptotic value, and we should emphasize that the cost per MW of these large floating farms is 25% cheaper than the cost of bottom-fixed farms (*ibid*, p. 718). In the case of bathymetric intervals, the Hywind and WindFloat designs record a very constant LCOE versus depth, but Hywind is 18 % cheaper

than WindFloat. At a depth of 0-200 m the TLB design would involve the lowest cost, but above 250 m its cost increases exponentially. It therefore seems that again the Hywind design would be the best option for the whole area considered because of the advantages of mass production. Another important parameter for LCOE involves distance to the shore: all the designs record almost parallel linear increases with distance, with a slope of more than 10 euro/MWh per 100 km. In our two cases, the maximum distances from the shore are at Cabo Begur, but they are only around 25-30 km, and the LCOE would be below 150 euro/MWh.

5. Conclusions and future outlook

In this paper, the wind energy resource has been estimated for the West Mediterranean using different models: ERAI and two WRF runs, one with data assimilation (D) and the other without (N). The WRF runs yield results with a 15x15 km resolution that better represents the topography and land-sea mask over the area. **Additionally, the study has been developed at different turbine heights given by the WRF runs. As far as we know, this is the first time that WRF wind outputs at different heights (at 70, 130 and 180 m) are computed for wind energy resource assessment with different real turbines. This method can be applied for other turbines in the future.**

Our novel method of estimation also opens another new research way for the future at different heights: the contribution of air density in the wind energy potential. This is not important for annual production, but for seasonal or monthly production could be very relevant, since hight pressures and cold temperatures can increment air density more than 10% with respect to the standard air density (ρ_0). This means an analogous energy production increment that can be computed by advanced atmospheric models like WRF with data assimilation.

The use of 3DVAR assimilation improves the representation of wind field using WRF over the ocean when compared with the simulations without data assimilation. In general, 3DVAR produces more realistic wind fields reducing the bias that appears when data assimilation is not used (the N experiment). This means that wind potential is more accurately computed when 3DVAR is used, leading to reduced estimations of the available wind resource. The results also indicate that D outperforms ERAI at estimating the wind resource, although not overwhelmingly so. When the wind potential of this area obtained with the D integration is compared to the simple estimation from ERAI data, the following advantages have been detected:

1. The average bias is smaller
2. ERAI tends to overestimate its performance at representing the wind field over the Western Mediterranean area. Hence D is more reliable.
3. D has a higher spatial resolution than ERAI, and it is better at capturing small-scale details, such as breezes or extreme and high values.

After determining which integration performs best, the results of D have been used to characterize the wind energy potential for the area. Total production and CF have been calculated for three different turbines. The CFs for wind energy production show that CF is not constant for the area, and has a seasonal behaviour with higher values in winter. In the north (Cabo Begur), a total number of 6840 turbines installed at 200 m intervals in shallow waters, over an area of $2318 km^2$ with an installed capacity of around 16.4 GW, could produce 55.8 TWh. The average CF in this area is 0.46, which is a very high value for wind energy. In the area around Menorca, a fewer number of turbines could be installed -1700- with a total capacity of 8.79 TWh, and a smaller mean CF of 0.30

A study of this area has shown that the simple use of ERAI clearly outperforms WRF integration without data assimilation (N), thus indicating that only a full 3DVAR integration can be an improvement if wind resources are to be accurately estimated for a given area. Nevertheless, it is to be noted that D and ERAI are very close to the observational error associated with the discrepancies between two observational sources: in-situ measurements from buoys and CCMPv2 gridded analysis.

In a previous work, a similar approach was carried out by this research team for another area of the Iberian Peninsula, using ERA40 instead of ERAI [30]. It was reported that the improvement through implementing a full 3DVAR integration with WRF was far more evident. With ERA40 being the previous generation of the ERAI reanalysis, this indicates that the data assimilation algorithms implemented in ERAI regarding the wind field are an important step forward. Future ECMWF reanalysis such as ERA5, with a higher resolution and improved assimilation algorithms, may render any WRF run unnecessary, even with data assimilation, unless a much higher spatial resolution can be achieved in the mesoscale model run.

6. Acknowledgments

This work has been funded by the Spanish Government's MINECO project CGL2016-76561-R (MINECO/FEDER EU), the University of the Basque Country (project GIU14/03) and the Basque Government (Elkartek 2017 INFORMAR project). The ECMWF ERA-Interim data used in this study have been obtained from the ECMWF-MARS Data Server thanks to agreements with ECMWF and AEMET. The authors would like to express their gratitude to the Spanish Port Authorities (Puertos del Estado) for kindly providing data for this study. The computational resources used in the project were provided by I2BASQUE. The authors thank the creators of the WRF/ARW and WRFDA systems for making them freely available to the community. NOAA_OI_SST_V2 data provided by the NOAA/OAR/ESRL PSD, Boulder, Colorado, USA, through their web-site at http://www.esrl.noaa.gov/psd/ was used in this paper. National Centers for Environmental Prediction/National Weather Service/NOAA/U.S. Department of Commerce. 2008, updated daily. NCEP ADP Global Upper Air and Surface Weather Observations (PREPBUFR format), May 1997 - Continuing. Research Data Archive at the National Center for Atmospheric Research, Computational and Information Systems Laboratory. http://rda.ucar.edu/datasets/ds337.0/ were used. All the calculations have been carried

out in the framework of R Core Team (2016). R: A language and environment for statistical computing. R Foundation for Statistical Computing, Vienna, Austria. URL https://www.R-project.org/.

References

[1] M. Esteban, D. Leary, Current developments and future prospects of offshore wind and ocean energy, Applied Energy 90 (1) (2012) 128–136.

[2] Statoil Company. 2016-11-20. URL: https://www.statoil.com/en/news/hywindscotland.html (2016).

[3] G. Gaudiosi, Offshore wind energy in the world context, Renewable Energy 9 (1) (1996) 899–904.

[4] European Wind Energy Association and Greenpeace. Wind Energy, 12. (2004).

[5] A. Myhr, C. Bjerkseter, A. Ågotnes, T. A. Nygaard, Levelised cost of energy for offshore floating wind turbines in a life cycle perspective, Renewable Energy 66 (2014) 714–728.

[6] A. Garrad, B. Adams, H. Matthies, M. Scherweit, T. Siebers, An assessment of the offshore wind potential in the EC, in: Proceedings of 15th British Wind Energy Conference, 1993, pp. 401–406.

[7] N. G. Mortensen, L. Landberg, I. Troen, E. Lundtang Petersen, Wind Atlas Analysis and Application program (WAsP): Vol. 1: Getting started, Tech. rep., Risø National Laboratory (1993).

[8] C. B. Hasager, R. J. Barthelmie, M. B. Christiansen, M. Nielsen, S. Pryor, Quantifying offshore wind resources from satellite wind maps: study area the North Sea, Wind Energy 9 (1-2) (2006) 63–74.

[9] P. Doubrawa, R. J. Barthelmie, S. C. Pryor, C. B. Hasager, M. Badger, I. Karagali, Satellite winds as a tool for offshore wind resource assessment: The Great Lakes Wind Atlas, Remote Sensing of Environment 168 (2015) 349–359.

[10] A. Yamaguchi, T. Ishihara, Assessment of offshore wind energy potential using mesoscale model and geographic information system, Renewable Energy 69 (2014) 506–515.

[11] M. J. Dvorak, C. L. Archer, M. Z. Jacobson, California offshore wind energy potential, Renewable Energy 35 (6) (2010) 1244–1254.

[12] M. S. Gross, V. Magar, Offshore wind energy potential estimation using UPSCALE climate data, Energy Science & Engineering 3 (4) (2015) 342–359.

[13] S. A. Akdağ, Ö. Güler, Evaluation of wind energy investment interest and electricity generation cost analysis for Turkey, Applied Energy 87 (8) (2010) 2574–2580.

[14] N. Fueyo, Y. Sanz, M. Rodrigues, C. Montañés, C. Dopazo, High resolution modelling of the on-shore technical wind energy potential in Spain, Wind energy 13 (8) (2010) 717–726.

[15] R. Pielke, W. Cotton, R. e. a. Walko, C. J. Tremback, W. A. Lyons, L. Grasso, M. Nicholls, M. Moran, D. Wesley, T. Lee, et al., A comprehensive meteorological modeling system RAMS, Meteorology and Atmospheric Physics 49 (1-4) (1992) 69–91.

[16] J. Winterfeldt, B. Geyer, R. Weisse, Using QuikSCAT in the added value assessment of dynamically downscaled wind speed, International Journal of Climatology 31 (7) (2011) 1028–1039. doi:10.1002/joc.2105.
URL `http://dx.doi.org/10.1002/joc.2105`

[17] N. Fueyo, Y. Sanz, M. Rodrigues, C. Montañés, C. Dopazo, The use of cost-generation curves for the analysis of wind electricity costs in Spain, Applied Energy 88 (3) (2011) 733–740.

[18] D. Carvalho, A. Rocha, C. S. Santos, R. Pereira, Wind resource modelling in complex terrain using different mesoscale–microscale coupling techniques, Applied Energy 108 (2013) 493–504.

[19] D. Carvalho, A. Rocha, M. Gómez-Gesteira, C. Santos, A sensitivity study of the WRF model in wind simulation for an area of high wind energy, Environmental Modelling & Software 33 (2012) 23–34.

[20] D. Carvalho, A. Rocha, M. Gómez-Gesteira, C. S. Santos, Sensitivity of the WRF model wind simulation and wind energy production estimates to planetary boundary layer parameterizations for onshore and offshore areas in the Iberian Peninsula, Applied Energy 135 (2014) 234–246.

[21] D. Carvalho, A. Rocha, M. Gómez-Gesteira, C. S. Santos, Comparison of reanalyzed, analyzed, satellite-retrieved and NWP modelled winds with buoy data along the Iberian Peninsula coast, Remote Sensing of Environment 152 (2014) 480–492.

[22] D. Carvalho, A. Rocha, M. Gómez-Gesteira, C. S. Santos, WRF wind simulation and wind energy production estimates forced by different reanalyses: Comparison with observed data for Portugal, Applied Energy 117 (2014) 116–126.

[23] D. Carvalho, A. Rocha, M. Gómez-Gesteira, C. S. Santos, Offshore wind energy resource simulation forced by different reanalyses: Comparison with observed data in the Iberian Peninsula, Applied Energy 134 (2014) 57–64.

[24] A. Pea, A. N. Hahmann, Atmospheric stability and turbulence fluxes at Horns Revan intercomparison of sonic, bulk and WRF model data, Wind Energy 15 (5) (2012) 717–731. doi:10.1002/we.500.
URL http://dx.doi.org/10.1002/we.500

[25] M. L. Aitken, B. Kosović, J. D. Mirocha, J. K. Lundquist, Large eddy simulation of wind turbine wake dynamics in the stable boundary layer using the weather research and forecasting model, Journal of Renewable and Sustainable Energy 6 (3) (2014) 033137.

[26] J. Zhao, Z.-H. Guo, Z.-Y. Su, Z.-Y. Zhao, X. Xiao, F. Liu, An improved multi-step forecasting model based on wrf ensembles and creative fuzzy systems for wind speed, Applied Energy 162 (2016) 808 – 826. doi:http://dx.doi.org/10.1016/j.apenergy.2015.10.145.
URL http://www.sciencedirect.com/science/article/pii/S0306261915013872

[27] J. Zhao, Y. Guo, X. Xiao, J. Wang, D. Chi, Z. Guo, Multi-step wind speed and power forecasts based on a wrf simulation and an optimized association method, Applied Energy 197 (2017) 183 – 202. doi:http://dx.doi.org/10.1016/j.apenergy.2017.04.017.
URL http://www.sciencedirect.com/science/article/pii/S0306261917304105

[28] P. de Jong, R. Dargaville, J. Silver, S. Utembe, A. Kiperstok, E. A. Torres, Forecasting high proportions of wind energy supplying the brazilian northeast electricity grid, Applied Energy 195 (2017) 538 – 555. doi:http://dx.doi.org/10.1016/j.apenergy.2017.03.058.
URL http://www.sciencedirect.com/science/article/pii/S0306261917302726

[29] P. M. Soares, D. C. Lima, R. M. Cardoso, M. L. Nascimento, A. Semedo, Western iberian offshore wind resources: More or less in a global warming climate?, Applied Energy 203 (2017) 72 – 90. doi:http://dx.doi.org/10.1016/j.apenergy.2017.06.004.
URL http://www.sciencedirect.com/science/article/pii/S0306261917307535

[30] A. Ulazia, J. Sáenz, G. Ibarra-Berastegui, Sensitivity to the use of 3DVAR data assimilation in a mesoscale model for estimating offshore wind energy potential. A case study of the Iberian northern coastline, Applied Energy 180 (2016) 617–627.

[31] M. Menendez, M. García-Díez, L. Fita, J. Fernández, F. J. Méndez, J. M. Gutiérrez, High-resolution sea wind hindcasts over the Mediterranean area, Climate Dynamics 42 (7) (2014) 1857–1872. doi:10.1007/s00382-013-1912-8.
URL http://dx.doi.org/10.1007/s00382-013-1912-8

[32] R. W. Reynolds, N. A. Rayner, T. M. Smith, D. C. Stokes, W. Wang, An improved in situ and satellite SST analysis for climate, Journal of climate 15 (13) (2002) 1609–1625.

[33] P. A. Mooney, F. J. Mulligan, R. Fealy, Evaluation of the sensitivity of the Weather Research and Forecasting Model to parameterization schemes for regional climates of europe over the period 199095, Journal of Climate 26 (3) (2013) 1002–1017. arXiv:http://dx.doi.org/10.1175/JCLI-D-11-00676.1, doi:10.1175/JCLI-D-11-00676.1.
URL http://dx.doi.org/10.1175/JCLI-D-11-00676.1

[34] D. P. Dee, S. M. Uppala, A. J. Simmons, P. Berrisford, P. Poli, S. Kobayashi, U. Andrae, M. A. Balmaseda, G. Balsamo, P. Bauer, P. Bechtold, A. C. M. Beljaars, L. van de Berg, J. Bidlot, N. Bormann, C. Delsol, R. Dragani, M. Fuentes, A. J. Geer, L. Haimberger, S. B. Healy, H. Hersbach, E. V. Hlm, L. Isaksen, P. Kllberg, M. Khler, M. Matricardi, A. P. McNally, B. M. Monge-Sanz, J.-J. Morcrette, B.-K. Park, C. Peubey, P. de Rosnay, C. Tavolato, J.-N. Thpaut, F. Vitart, The ERA-Interim reanalysis: configuration and performance of the data assimilation system, Quarterly Journal of the Royal Meteorological Society 137 (656) (2011) 553–597. doi:10.1002/qj.828.
URL http://dx.doi.org/10.1002/qj.828

[35] P.P.E., Puertos del Estado: Oceanography: Forecast, real time and climate, Spanish Government:

Madrid. Updated 2015-10-11. http://www.puertos.es/en-us/oceanografia/Pages/portus.aspx.
[36] NASA/GSFC/NOAA. Cross-Calibrated Multi-Platform Ocean Surface Wind Vector L3.0 First-Look Analyses. Ver. 1. PO.DAAC, CA, USA. Dataset accessed [2015-11-01] at http://dx.doi.org/10.5067/CCF30-01XXX (2009).
[37] ETOPO1. 2-minute Gridded Global Relief data (ETOPO2v2), NOAA, National Geophysical Data Center, Boulder, Colorado. 2006.
[38] W. C. Skamarock, J. B. Klemp, J. Dudhia, D. O. Gill, D. M. Barker, M. G. Duda, X.-Y. Huang, W. Wang, J. G. Powers, et al., A description of the advanced research WRF version 3, NCAR Technical note 475 (2008) 113.
[39] R. Jones, J. Murphy, M. Noguer, Simulation of climate change over europe using a nested regional-climate model. I: Assessment of control climate, including sensitivity to location of lateral boundaries, Quarterly Journal of the Royal Meteorological Society 121 (526) (1995) 1413–1449.
[40] M. Rummukainen, State-of-the-art with regional climate models, Wiley Interdisciplinary Reviews: Climate Change 1 (1) (2010) 82–96. doi:10.1002/wcc.8.
[41] R. Reynolds, T. Smith, L. Chunying, D. B. Chelton, K. S. Casey, M. G. Schlax, Daily high-resolution-blended analyses for sea surface temperature, J. Climate 20 (2007) 5473–5496.
[42] D. Barker, X.-Y. Huang, Z. Liu, T. Auligné, X. Zhang, S. Rugg, R. Ajjaji, A. Bourgeois, J. Bray, Y. Chen, et al., The weather research and forecasting model's community variational/ensemble data assimilation system: WRFDA, Bulletin of the American Meteorological Society 93 (6) (2012) 831–843.
[43] E. Kalnay, Atmospheric modeling, data assimilation and predictability, Cambridge university press, 2003.
[44] D. F. Parrish, J. C. Derber, The National Meteorological Center's spectral statistical-interpolation analysis system, Monthly Weather Review 120 (8) (1992) 1747–1763.
[45] K. E. Taylor, Summarizing multiple aspects of model performance in a single diagram, Journal of Geophysical Research: Atmospheres 106 (D7) (2001) 7183–7192.
[46] S. Hsu, Estimating overwater friction velocity and exponent of power-law wind profile from gust factor during storms, Journal of Waterway, Port, Coastal, and Ocean Engineering 129 (4) (2003) 174–177.
[47] D. Haugen, Workshop on Micrometeorology, Amer. Meteor. Soc. (1973) 392.
[48] G. M. Masters, Renewable and efficient electric power systems, John Wiley & Sons, 2013.
[49] C. Lavalle, C. Rocha Gomes, C. Baranzelli, F. Batista e Silva, Coastal Zones. Policy alternatives impacts on European Coastal Zones, 2000 2050, Joint Research Centre Institute for Environment and Sustainability, 2011.
[50] C. P. Butterfield, W. Musial, J. Jonkman, P. Sclavounos, L. Wayman, Engineering challenges for floating offshore wind turbines, National Renewable Energy Laboratory Golden, CO, USA, 2007.
[51] M. Bahrman, B. Johnson, The ABCs of HVDC transmission technologies, IEEE Power and Energy Magazine 2 (5) (2007) 32–44.
[52] GWEC, Report. Global Wind Energy Council (GWEC), 2009 (www.gwec.net accesed 22.06.09).
[53] Gorona del Viento. 2017-1-20. URL: http://www.goronadelviento.es/index.php (2017).
[54] Menorca Info. 2017-1-20. URL: https://menorca.info/hilo/prospecciones.html (2017).
[55] Red Elctrica Espaola. 2017-1-20. URL: http://www.ree.es/es/balance-diario/baleares/2017/01/31 (2017).
[56] Red Eléctrica de España. Informe: El sistema eléctrico español, 2015. URL: http://www.ree.es/sites/default/files/downloadable/inf$_s is_elec_ree_2015.pdf$(2015).